optica

Silicon photonic transmitter for polarization-encoded quantum key distribution

CHAOXUAN MA,[1,†,*] WESLEY D. SACHER,[1,2,†] ZHIYUAN TANG,[3,†] JARED C. MIKKELSEN,[1] YISU YANG,[1]
FEIHU XU,[1,4] TORREY THIESSEN,[1] HOI-KWONG LO,[1,3] AND JOYCE K. S. POON[1,5]

[1]Department of Electrical and Computer Engineering, University of Toronto, 10 King's College Road, Toronto, Ontario M5S 3G4, Canada
[2]Departments of Physics & Applied Physics, California Institute of Technology, 1200 E. California Blvd., Pasadena, California 91125, USA
[3]Department of Physics, University of Toronto, 60 St. George St., Toronto, Ontario M5S 1A7, Canada
[4]Research Laboratory of Electronics, Massachusetts Institute of Technology, 77 Massachusetts Ave., Cambridge, Massachusetts 02139, USA
[5]e-mail:joyce.poon@utoronto.ca
*Corresponding author: chaoxuan.ma@mail.utoronto.ca

Received 6 June 2016; revised 30 August 2016; accepted 5 October 2016 (Doc. ID 267802); published 31 October 2016

Silicon (Si) photonics is forming a fabless ecosystem, which is enabling low-cost and densely integrated components for optical communications and quantum information. We present a Si optical transmitter for polarization-encoded quantum key distribution (QKD). The chip was fabricated in a standard Si photonic foundry process and integrated together a pulse generator, intensity modulator, variable optical attenuator, and polarization modulator in a 1.3 mm × 3 mm die area. The devices in the photonic circuit meet the requirements for QKD. The transmitter was used in a proof-of-concept demonstration of the BB84 QKD protocol over a 5 km long fiber link. This work shows the potential of using foundry Si photonics for low-cost, wafer-scale fabricated components for quantum information.

OCIS codes: (130.0130) Integrated optics; (250.5300) Photonic integrated circuits; (270.5568) Quantum cryptography.

http://dx.doi.org/10.1364/OPTICA.3.001274

1. INTRODUCTION

Leveraging the infrastructure for complementary metal–oxide–semiconductor (CMOS) electronics manufacturing, silicon (Si) photonics is emerging as a key technology for next-generation computing and communication systems, with low power consumption and potentially low-cost optoelectronic integration. Many Si photonic devices for classical optical communication have been demonstrated, including waveguides, high-speed optical modulators, photodetectors, wavelength converters, and polarization management components [1–3]. These building blocks, along with photon sources in Si and hybrid integration methods for single-photon detectors, pave the way for Si photonics to be applied to quantum information [4,5]. Quantum photonics has traditionally relied on bulk optical devices or exquisitely fabricated, singular microphotonic devices that have limited scalability and integration compatibility with other classical computing or communication components. Foundry fabrication services can enable Si photonic integrated circuits (PICs) for quantum information [2], reducing the cost of incorporating quantum photonic functionality into classical systems.

A quantum technology prime for widespread use is quantum key distribution (QKD) [6,7], which exploits statistics of single photons to generate secure encryption keys. Owing to the quantum no-cloning theorem [8], inevitable disturbance introduced by eavesdropping leads to a higher-than-expected quantum bit error rate (QBER) that can be detected. Moreover, unconditional security with faint laser pulses can be achieved using decoy states [9–12]. Most of today's commercial QKD systems use discrete components [13,14]. For chip-scale devices, silica planar lightwave circuits have been used for passive interferometers and waveguides [15–18]. Recently, phase-shift and time-bin encoded QKD have been demonstrated using transmitter and receiver PICs (without the single-photon detectors) fabricated in indium phosphide (InP) and silicon nitride (SiN) integrated photonic platforms available through foundries [19].

In this article, we report on, to our knowledge, the first transmitter PIC for QKD fabricated in a standard foundry Si photonic platform. The large wafer sizes available in Si photonic foundry processes (8" or 12" diameters [2,20] versus 3" for InP [21] and 4" for SiN [22]) and dense integration are conducive to scaling to high-volume manufacturing. The transmitter PIC supports polarization-encoded QKD protocols and contains ring modulators, a variable optical attenuator (VOA), and polarization modulator. A secret key rate of 0.952 kbps was achieved with a QBER of 5.4% in a proof-of-concept QKD demonstration with the BB84 protocol and using some bulk components. Phase and time-bin encoding should also be possible using Si photonics, but such implementations require interferometers with long delay lines.

Even though polarization states are not maintained in standard single-mode fibers, the relations between the polarizations are preserved at the receiver, so the states can be recovered.

2334-2536/16/111274-05 Journal © 2016 Optical Society of America

Polarization division multiplexing is becoming prevalent in optical communication [23,24]. Polarization-encoded QKD has been achieved over 200 km of standard fibers [25], and real-time polarization control for QKD has also been shown [26]. Polarization-encoded QKD is also preferred for free-space, e.g., satellite-to-ground, links [27–29]. Recently, on-chip path-encoding single-photon states have been shown to be translated into polarization-encoded states in fibers [30,31].

2. QKD TRANSMITTER PIC

The schematic and optical micrographs of the PIC are shown in Fig. 1. The transmitter, with a small size of $1.3 \times 3\ \mathrm{mm}^2$, was fabricated in the A*STAR IME Baseline Si Photonics process. It integrates two identical ring modulators, a variable optical attenuator and a polarization modulator. The first ring modulator generates periodic nanosecond (ns) pulse trains, while the second ring modulates the intensity to create decoy and signal states if needed. The VOA attenuates the pulses to the single-photon level, and the polarization modulator prepares the polarization states. Light is coupled into/out of the chip using on-chip adiabatic taper waveguide couplers and lensed fibers with a 2.5 μm spot diameter. The tip of the edge couplers has a cross-section of 200 nm × 220 nm so as to minimize the polarization-dependent loss (PDL). Extra input and output ports in the PIC enable the characterization of the individual devices.

A. Microring Modulators

Figure 2(a) shows the schematic of the microring modulator. Each microring contains a 400 μm long PIN diode phase-shifter inside the ring for modulation. A 2 × 2 Mach–Zehnder interferometer (MZI) coupler and an intracavity 100 μm long doped Si resistive heater provide independent tuning of the coupling coefficient and resonance wavelength, respectively, to achieve modulation with a high extinction ratio (ER). Figure 2(b) shows the static transmission of the transmitter when both microrings were set to the critical coupling condition and slightly detuned from each other. The microrings had a free spectral range of 0.65 nm, and the minimum transmission was about −27 dB. The intrinsic Q factor of the microrings was about 1.9×10^6. Figure 2(c) shows the tuning of the transmission at a fixed wavelength of 1549.9 nm as a DC voltage was applied to the intracavity PIN diode of one of the microrings. A static ER of 25.6 dB was achieved by an applied voltage of only 50 mV. Figure 2(d) shows the pulse shape generated by the first microring, which is a histogram of 8000 overlapping pulses. The microring was driven by a programmable pattern generator with bursts of 8000 1 ns wide pulses at a repetition rate of 10 MHz to generate a train of nominally identical pulses. The tests lasted for >5 min. The optical pulses had a full width half maximum (FWHM) of 2.4 ns and the jitter was 1.2 ns. The dynamic ER was 20 dB, which, to our knowledge, is the highest of any Si microring and Mach–Zehnder modulator. A high ER reduces the QBER penalty [6].

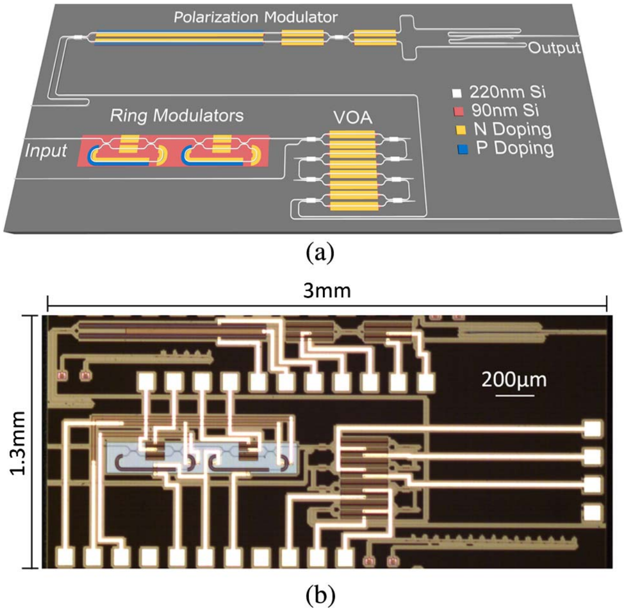

Fig. 1. (a) Schematic of the Si PIC transmitter for polarization-encoded QKD. The transmitter consists of a microring pulse generator, microring intensity modulator, VOA, and polarization controller. (b) Optical micrograph of the chip.

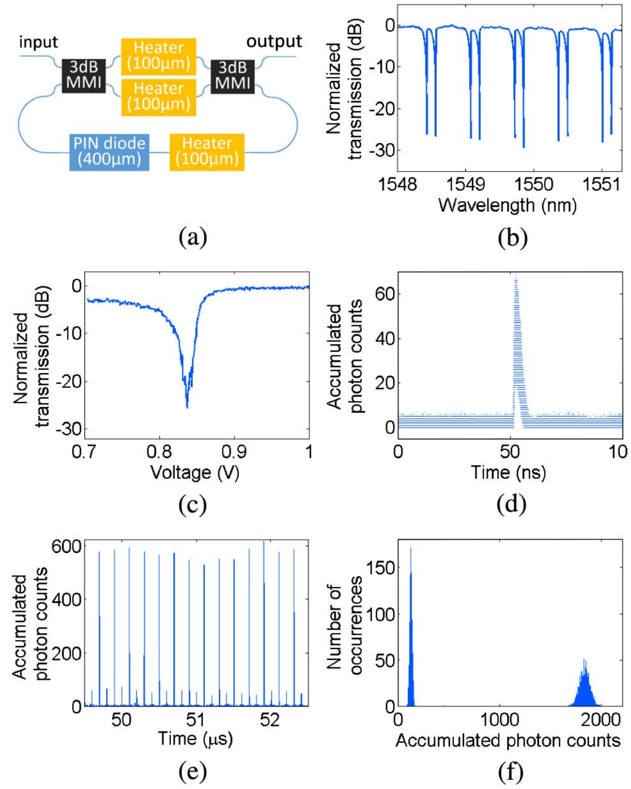

Fig. 2. (a) Schematic of the microring modulator. (b) Normalized transmission spectrum with both microrings set at critical coupling. (c) Tuning of the transmission. (d) Histogram of 8000 overlapping pulses generated by the first microring. (e) Time-dependent accumulated photon counts due to alternating intensities from the modulation of the two microrings. The time bin is 1 ns. (f) Photon number distribution of the pulses in (e) calculated using a time bin of 5 ns.

The two microring modulators, when tuned to matched resonances, could generate pulses with varying amplitude levels. Figure 2(e) shows the cumulative photon count of 3.75×10^5 repetitions of a modulation pattern with alternating intensities. The first microring was driven with 1 ns long pulses at a repetition rate of 10 MHz and the second microring modulator was driven by a 5 MHz square-wave from an arbitrary function generator (AFG).

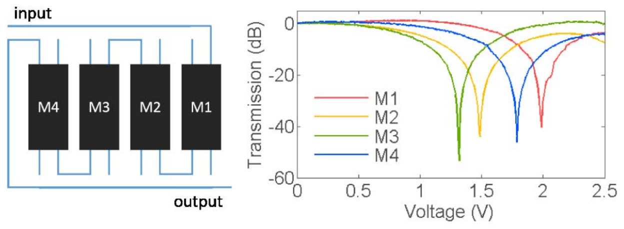

(a) (b)

Fig. 3. (a) Schematic of the VOA. The VOA is a cascade of four identical MZIs (labeled M1 to M4). (b) Normalized transmission of each MZI at 1550 nm. The maximum attenuation provided by each MZI is 40.3, 44.0, 53.3, and 46.4 dB. The transmission is normalized to the starting point (zero bias).

The two voltage levels of the AFG produced the two intensities, as shown in Fig. 2(e). Varying intensities can be used for signal and decoy states. Figure 2(f) shows the cumulative photon count distribution. The per-pulse mean photon numbers for the two states were 0.14 ± 0.0036 and 0.01 ± 0.0009, respectively.

B. Variable Optical Attenuator

The next device in the PIC is the VOA, consisting of four cascaded and nominally balanced 2×2 MZIs. Each MZI has two 3 dB multimode interference couplers separated by 300 μm long phase-shifters, each containing a 250 μm long heater. The attenuation is tuned by the differential phase shifts in the MZIs. The tuning ranges of the MZIs at 1550 nm (labeled M1 to M4) are shown in Fig. 3(b). Each MZI could provide >40 dB of attenuation.

C. Polarization Modulator

The output of the VOA connects to the polarization modulator, which is used to prepare the states, $\{|H\rangle, |V\rangle, |D\rangle, |A\rangle\}$, that constitute the two conjugate bases, with $|D\rangle = \frac{1}{\sqrt{2}}(|H\rangle + |V\rangle)$ and $|A\rangle = \frac{1}{\sqrt{2}}(|H\rangle - |V\rangle)$. In polarization encoding, the states are identified as the polarization angles {0°, 90°, 45°, −45°}. A schematic of the polarization modulator is shown in Fig. 4(a), and the design is based on Ref. [32]. The polarization modulator consists of a nominally balanced MZI and a polarization rotator combiner (PRC). The Si PIC preferentially supports the fundamental transverse electric mode (TE0). In the polarization modulator, the MZI controls the amplitude ratio between the two inputs to the PRC. Then the PRC converts the TE0 mode in one of its inputs (e.g., the lower branch) into the fundamental transverse magnetic (TM0) mode, which is combined with the TE0 light from the other input (e.g., the top branch) at the output.

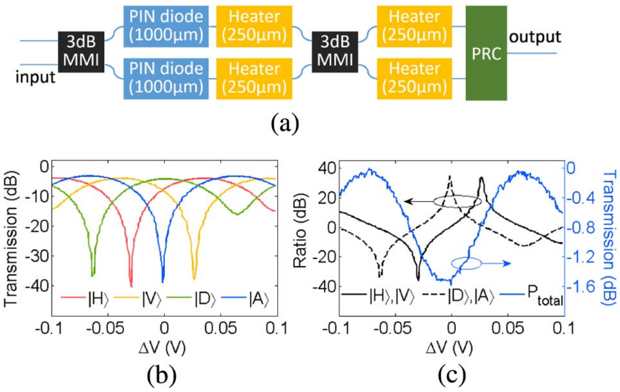

(a)

(b) (c)

Fig. 4. (a) Schematic of the polarization modulator. (b) Normalized transmission of the polarizations versus PIN diode voltage in the MZI, $\pm\Delta V$, at a bias of 1.2 V. (c) Total transmitted power (normalized) and power ratio in each basis versus ΔV.

The MZI has a 1000 μm long PIN diode and a 250 μm long resistive heater in each phase-shifter. Heaters at the inputs to the PRC enable phase tuning between the TE and TM components. The PIN diodes are driven in push-pull to modulate the waveguide effective index. Ideally, only the real part of the index is modified, but the plasma dispersion effect also slightly alters the absorption [33], which causes a slight PDL. The effect of the coupling between the real and imaginary parts of the refractive index change is described in the Supplement 1. PDL can also be caused by fabrication errors in the PRC and the edge couplers. The PDL at the output can be compensated by adding tunable attenuators at the inputs of the PRC for fine balancing of the loss between the TE and TM components. The polarization extinction ratio (PER) can be increased by including PIN diode phase-shifters at the inputs of PRC to dynamically compensate for the phase mismatch between the two polarizations.

To measure the polarization tunability, the output of the polarization modulator was passed through a fused fiber polarization-independent 3 dB splitter, and each output passed through an in-fiber polarization controller (PC) and a fiber-based polarization beam splitter (PBS). The PCs were set such that each PBS was aligned to the rectilinear and diagonal bases, respectively. Figure 4(b) shows the transmission for 1550 nm at the outputs of each PBS versus a small-signal voltage sweep, ΔV, applied in push-pull mode to the PIN diodes in the on-chip polarization controller at a 1.2 V bias. Figure 4(c) shows the total transmitted power and power ratio of the two orthogonal components in each basis. The PER was >30 dB, and the power variation across the polarization states was 0.9 dB.

To illustrate the capability to generate variable amplitude levels (e.g., for decoy states [10]), attenuation, and polarization modulation, Fig. 5 shows the photon number histograms of the four polarizations projected onto $|D\rangle$ using the second microring modulator, VOA, and polarization modulator. The input to the chip was a periodic pulse train to reduce the onus of stabilizing two microrings. The mean photon numbers for the two intensities were about 0.094 and 0.029. This measurement was carried out using the setup in Fig. 6, which is described in detail in the next section.

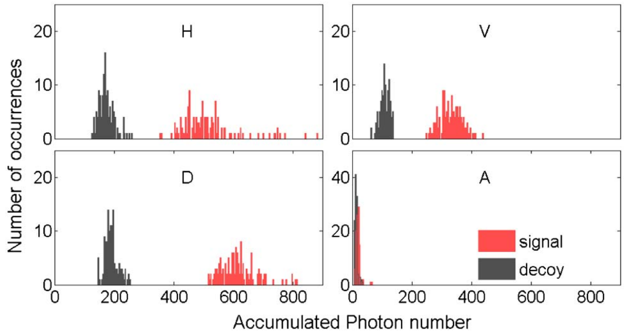

Fig. 5. Projections of the polarization states onto $|D\rangle$ showing multi-level modulation using the second microring, VOA, and polarization modulator.

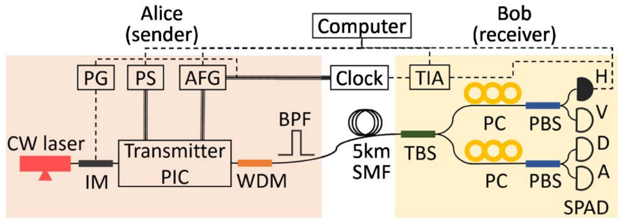

Fig. 6. Setup schematic. PS, power supply; PG, pulse generator; IM, intensity modulator; AFG, arbitrary function generator; BPF, bandpass filter; SMF, single-mode fiber; TBS, tunable beam splitter; PC, polarization controller; PBS, polarization beam splitter; SPAD, single-photon avalanche photodetector; TIA, time interval analyzer.

3. QUANTUM KEY DISTRIBUTION

Lastly, we present a proof-of-concept BB84 QKD demonstration using the on-chip VOA and polarization modulator at a wavelength of 1550 nm. The setup is shown in Fig. 6. For improved modulation ER and thermal stability, the microrings were bypassed and an external $LiNbO_3$ intensity modulator was used instead (i.e., no decoy states were generated). The external modulator provided a dynamic ER of 30 dB (versus 20 dB for the microring), reducing the QBER penalty. For a perfect single-photon source, a secret key with Shor–Preskill's proof [34] requires a QBER $\lesssim 11\%$, but secure QKD can be done with weak coherent pulses [35]. At the sender (Alice's) side, the input to the PIC was bursts of 1000 optical pulses with a FWHM of 1 ns at a repetition rate of 10 MHz. The bursts were at the clock rate of 9.71 kHz. The PIC attenuated pulses to the single-photon level and prepared the four polarization states according to 1000 prestored, uniformly distributed pseudo-random numbers generated by the randi function in MATLAB. A wavelength division multiplexer (WDM) and a bandpass filter (BPF) were added at the PIC output to remove the weak electroluminescence near a wavelength 1150 nm from the forward-biased PIN diodes [36]. The spectral and electrical characteristics of this electroluminescence in Si rib waveguides are described in the Supplement 1. The WDM and BPF added a loss of 5 dB and can be replaced by an integrated on-chip filter in the future.

The signals were transmitted over 5 km of standard single-mode fiber. At the receiver (Bob's) side, a tunable beam splitter balanced the losses of two paths, so each basis has a 50% probability to be chosen for the measurement. The PC preceding each PBS was tuned for the measurement of the two conjugated bases in the two paths, and the photons were detected using InGaAs single-photon avalanche photodetectors (SPADs). The detection efficiency of the SPADs was 20% and the dead time was 15 μs. The four channels at Bob's end were measured sequentially to maintain the same detection efficiency. The link loss, which includes the fiber and Bob's equipment but not the detector efficiency, was ~6.1 dB. The time interval analyzer was synchronized with the clock to perform time-correlated single-photon counting. The on-chip VOA attenuated the pulse intensity by 27 dB. A total of 562 Mbits (effective) were emitted for each channel test. The photon fluxes for the four polarization states had a variation of ~1 dB, after accounting for the differences in connector loss, in agreement with the classical results. The mean photon per pulse is estimated to be 0.024 and the QBER is about 5.4%, which is sufficiently low for decoy-state implementations. The raw rate was 13.2 kbps and the asymptotic secure key rate was ~0.95 kbps, estimated using Eq. (12) in Ref. [10] without decoy states. Our simulations show that with one decoy state, our key rate can be increased to 4 kbps. The key rate would be improved with faster and higher-efficiency detectors and higher modulation speeds.

4. DISCUSSION

While our results show the basic feasibility of foundry Si photonics for QKD, significant opportunity exists for further development. For a fully integrated transmitter on Si, hybrid lasers can act as on-chip light sources [37], and active feedback control for stabilization is necessary [38]. Mach–Zehnder modulators (MZMs) can be used in lieu of microrings to be more robust against thermal fluctuations, though Si MZMs have higher loss than microrings and the highest ER has only been about 13 dB, albeit at >10 Gb/s modulation rates [39]. Higher ER should be achievable by operating close to the null transmission point of the MZM and by active control of the modulator phase *and loss* biases (due to the coupling between the real and imaginary parts of the refractive index change from the plasma dispersion effect) [40]. As mentioned in Section 2C, the PDL may be reduced by adding attenuators before the PRC. Further, an evaluation of the single-photon polarization states can be carried out using quantum-state tomography to more precisely assess the sources of imperfections in the polarization encoding [31].

A particularly formidable challenge in Si photonics is high-contrast spectral filters because the large refractive index difference between the waveguide core and cladding leads to sensitivity to phase variations and optical scattering from sidewall roughness. Fifth-order coupled microring filters can achieve contrasts >50 and 100 dB (using two stages) [41–43]. Such high-order filters, with a Vernier architecture, can be used to suppress the electroluminescence and pump light in nonlinear conversion processes. SiN-on-Si platforms may also be considered for low-loss waveguides and potentially lower crosstalk passives, which may also be useful for a quantum receiver [44].

5. CONCLUSION

In summary we have demonstrated the first Si PIC transmitter, to our knowledge, for polarization-encoded QKD. Proof-of-concept QKD demonstration shows a QBER of 5.4% and asymptotic secure key rate of 0.95 kbps. Future improvements include the incorporation of feedback and temperature control to stabilize the chip, compensating for the PDL, and receiver integration. This work shows the potential of using foundry Si photonics for low-cost, wafer-scale manufactured components for optical quantum information.

Funding. Natural Sciences and Engineering Research Council of Canada (NSERC); Canada Research Chairs; Canada Foundation for Innovation (CFI); Ontario Research Fund.

Acknowledgment. The fabrication was supported by CMC Microsystems. We thank Dr. D. Deptuck for his assistance during tapeout and Prof. L. Qian for the loan of the SPADs.

[†] These authors contributed equally to this work.

See Supplement 1 for supporting content.

REFERENCES

1. R. Soref, "The past, present, and future of silicon photonics," IEEE J. Sel. Top. Quantum Electron. **12**, 1678–1687 (2006).
2. A. E. J. Lim, J. Song, Q. Fang, C. Li, X. Tu, N. Duan, K. K. Chen, R. P. C. Tern, and T. Y. Liow, "Review of silicon photonics foundry efforts," IEEE J. Sel. Top. Quantum Electron. **20**, 405–416 (2014).
3. C. R. Doerr, "Silicon photonic integration in telecommunications," Front Phys. **3**, 37 (2015).
4. D. Bonneau, J. W. Silverstone, and M. G. Thompson, "Silicon quantum photonics," in *Silicon Photonics III* (Springer, 2016), pp. 41–82.
5. J. Silverstone, D. Bonneau, J. O. Brien, and M. Thompson, "Silicon quantum photonics," IEEE J. Sel. Top. Quantum Electron. **22**, 1–13 (2016).
6. N. Gisin, G. Ribordy, W. Tittel, and H. Zbinden, "Quantum cryptography," Rev. Mod. Phys. **74**, 145–195 (2002).
7. H.-K. Lo, M. Curty, and K. Tamaki, "Secure quantum key distribution," Nat. Photonics **8**, 595–604 (2014).
8. W. K. Wootters and W. H. Zurek, "A single quantum cannot be cloned," Nature **299**, 802–803 (1982).
9. W.-Y. Hwang, "Quantum key distribution with high loss: toward global secure communication," Phys. Rev. Lett. **91**, 057901 (2003).
10. H.-K. Lo, X. Ma, and K. Chen, "Decoy state quantum key distribution," Phys. Rev. Lett. **94**, 230504 (2005).
11. X. Ma, B. Qi, Y. Zhao, and H.-K. Lo, "Practical decoy state for quantum key distribution," Phys. Rev. A **72**, 012326 (2005).
12. X.-B. Wang, "Beating the photon-number-splitting attack in practical quantum cryptography," Phys. Rev. Lett. **94**, 230503 (2005).
13. ID Quantique, "Clavis2 QKD platform" (2016), http://www.idquantique.com/photon-counting/clavis2-qkd-platform/.
14. QuantumCTek, "Quantum gateway" (2016), http://www.quantum-info.com/en.php/Show/index/id/126.
15. Y. Nambu, K. Yoshino, and A. Tomita, "Quantum encoder and decoder for practical quantum key distribution using a planar lightwave circuit," J. Mod. Opt. **55**, 1953–1970 (2008).
16. Y. Nambu, T. Hatanaka, and K. Nakamura, "BB84 quantum key distribution system based on silica-based planar lightwave circuits," Jpn. J. Appl. Phys. **43**, L1109 (2004).
17. M. Kristensen, J. Maack, A. Thomasen, T. Balle, and J. Selchau, "Quantum key distribution using phase encoding in double-pass silica-on-silicon circuits with grating reflectors," in *Optical Sensors* (Optical Society of America, 2014), paper SeW4C.1.
18. G. Mélen, T. Vogl, M. Rau, G. Corrielli, A. Crespi, R. Osellame, and H. Weinfurter, "Integrated quantum key distribution sender unit for daily-life implementations," Proc. SPIE **9762**, 97620A 2016.
19. P. Sibson, C. Erven, M. Godfrey, S. Miki, T. Yamashita, M. Fujiwara, M. Sasaki, H. Terai, M. G. Tanner, C. M. Natarajan, R. H. Hadfield, J. L. O'Brien, and M. G. Thompson, "Chip-based quantum key distribution," arXiv:1509.00768 (2015).
20. F. Boeuf, S. Cremer, E. Temporiti, M. Fere, M. Shaw, N. Vulliet, B. Orlando, D. Ristoiu, A. Farcy, T. Pinguet, A. Mekis, G. Masini, P. Sun, Y. Chi, H. Petiton, S. Jan, J. R. Manouvrier, C. Baudot, P. L. Maitre, J. F. Carpentier, L. Salager, M. Traldi, L. Maggi, D. Rigamonti, C. Zaccherini, C. Elemi, B. Sautreuil, and L. Verga, "Recent progress in silicon photonics R&D and manufacturing on 300 mm wafer platform," in *Optical Fiber Communications Conference and Exhibition* (Optical Society of America, 2015), paper W3A–1.
21. M. Smit, X. Leijtens, H. Ambrosius, E. Bente, J. Van der Tol, B. Smalbrugge, T. De Vries, E.-J. Geluk, J. Bolk, R. Van Veldhoven, L. Augustin, P. Thijs, D. D'Agostino, H. Rabbani, K. Lawniczuk, S. Stopinski, S. Tahvili, A. Corradi, E. Kleijn, D. Dzibrou, M. Felicetti, E. Bitincka, V. Moskalenko, J. Zhao, R. Santos, G. Gilardi, W. Yao, K. Williams, P. Stabile, P. Kuindersma, J. Pello, S. Bhat, Y. Jiao, D. Heiss, G. Roelkens, M. Wale, P. Firth, F. Soares, N. Grote, M. Schell, H. Debregeas, M. Achouche, J.-L. Gentner, A. Bakker, T. Korthorst, D. Gallagher, A. Dabbs, A. Melloni, F. Morichetti, D. Melati, A. Wonfor, R. Penty, R. Broeke, B. Musk, and D. Robbins, "An introduction to InP-based generic integration technology," Semicond. Sci. Technol. **29**, 083001 (2014).
22. R. Heideman, A. Leinse, W. Hoving, R. Dekker, D. Geuzebroek, E. Klein, R. Stoffer, C. Roeloffzen, L. Zhuang, and A. Meijerink, "Large-scale integrated optics using triplex waveguide technology: from UV to IR," Proc. SPIE **7221**, 72210R 2009.
23. H. Sun, K.-T. Wu, and K. Roberts, "Real-time measurements of a 40 Gb/s coherent system," Opt. Express **16**, 873–879 (2008).
24. P. J. Winzer, A. H. Gnauck, C. R. Doerr, M. Magarini, and L. L. Buhl, "Spectrally efficient long-haul optical networking using 112-Gb/s polarization-multiplexed 16-QAM," J. Lightwave Technol. **28**, 547–556 (2010).
25. Y. Liu, T.-Y. Chen, J. Wang, W.-Q. Cai, X. Wan, L.-K. Chen, J.-H. Wang, S.-B. Liu, H. Liang, L. Yang, C.-Z. Peng, K. Chen, Z.-B. Chen, and J.-W. Pan, "Decoy-state quantum key distribution with polarized photons over 200 km," Opt. Express **18**, 8587–8594 (2010).
26. G. B. Xavier, N. Walenta, G. V. de Faria, G. P. Temporão, N. Gisin, H. Zbinden, and J. P. von der Weid, "Experimental polarization encoded quantum key distribution over optical fibres with real-time continuous birefringence compensation," New J. Phys. **11**, 045015 (2009).
27. T. Schmitt-Manderbach, H. Weier, M. Fürst, R. Ursin, F. Tiefenbacher, T. Scheidl, J. Perdigues, Z. Sodnik, C. Kurtsiefer, J. G. Rarity, A. Zeilinger, and H. Weinfurter, "Experimental demonstration of free-space decoy-state quantum key distribution over 144 km," Phys. Rev. Lett. **98**, 010504 (2007).
28. S. Nauerth, F. Moll, M. Rau, C. Fuchs, J. Horwath, S. Frick, and H. Weinfurter, "Air-to-ground quantum communication," Nat. Photonics **7**, 382–386 (2013).
29. J.-Y. Wang, B. Yang, S.-K. Liao, L. Zhang, Q. Shen, X.-F. Hu, J.-C. Wu, S.-J. Yang, H. Jiang, Y.-L. Tang, B. Zhong, H. Liang, W.-Y. Liu, Y.-H. Hu, Y.-M. Huang, B. Qi, J.-G. Ren, G.-S. Pan, J. Yin, J.-J. Jia, Y.-A. Chen, K. Chen, C.-Z. Peng, and J.-W. Pan, "Direct and full-scale experimental verifications towards ground-satellite quantum key distribution," Nat. Photonics **7**, 387–393 (2013).
30. L. Olislager, J. Safioui, S. Clemmen, K. P. Huy, W. Bogaerts, R. Baets, P. Emplit, and S. Massar, "Silicon-on-insulator integrated source of polarization-entangled photons," Opt. Lett. **38**, 1960–1962 (2013).
31. J. Wang, D. Bonneau, M. Villa, J. W. Silverstone, R. Santagati, S. Miki, T. Yamashita, M. Fujiwara, M. Sasaki, H. Terai, M. G. Tanner, C. M. Natarajan, R. H. Hadfield, J. L. O'Brien, and M. G. Thompson, "Chip-to-chip quantum photonic interconnect by path-polarization interconversion," Optica **3**, 407–413 (2016).
32. W. D. Sacher, T. Barwicz, B. J. Taylor, and J. K. Poon, "Polarization rotator-splitters in standard active silicon photonics platforms," Opt. Express **22**, 3777–3786 (2014).
33. R. A. Soref and B. R. Bennett, "Electrooptical effects in silicon," IEEE J. Quantum Electron. **23**, 123–129 (1987).
34. P. W. Shor and J. Preskill, "Simple proof of security of the BB84 quantum key distribution protocol," Phys. Rev. Lett. **85**, 441–444 (2000).
35. D. Gottesman, H.-K. Lo, N. Lütkenhaus, and J. Preskill, "Security of quantum key distribution with imperfect devices," Quantum Inf. Comput. **4**, 325–360 (2004).
36. T. Fuyuki, H. Kondo, T. Yamazaki, Y. Takahashi, and Y. Uraoka, "Photographic surveying of minority carrier diffusion length in polycrystalline silicon solar cells by electroluminescence," Appl. Phys. Lett. **86**, 262108 (2005).
37. D. Liang and J. E. Bowers, "Recent progress in lasers on silicon," Nat. Photonics **4**, 511–517 (2010).
38. F. Morichetti, S. Grillanda, and A. Melloni, "Breakthroughs in photonics 2013: toward feedback-controlled integrated photonics," IEEE Photon. J. **6**, 1–6 (2014).
39. K. Ogawa, K. Goi, Y. T. Tan, T.-Y. Liow, X. Tu, Q. Fang, G.-Q. Lo, and D.-L. Kwong, "Silicon Mach–Zehnder modulator of extinction ratio beyond 10 dB at 10.0–12.5 Gbps," Opt. Express **19**, B26–B31 (2011).
40. A. W. MacKay, "Complex phase biasing of silicon Mach–Zehnder interferometer modulators," Master's thesis (University of Toronto, 2014).
41. J. C. C. Mak, W. D. Sacher, T. Xue, J. C. Mikkelsen, Z. Yong, and J. K. S. Poon, "Automatic resonance alignment of high-order microring filters," IEEE J. Quantum Electron. **51**, 1–11 (2015).
42. P. Dong, N.-N. Feng, D. Feng, W. Qian, H. Liang, D. C. Lee, B. J. Luff, T. Banwell, A. Agarwal, P. Toliver, R. Menendez, T. K. Woodward, and M. Asghari, "GHz-bandwidth optical filters based on high-order silicon ring resonators," Opt. Express **18**, 23784–23789 (2010).
43. J. R. Ong, R. Kumar, and S. Mookherjea, "Ultra-high-contrast and tunable-bandwidth filter using cascaded high-order silicon microring filters," IEEE Photon. Technol. Lett. **25**, 1543–1546 (2013).
44. W. D. Sacher, Y. Huang, G.-Q. Lo, and J. K. S. Poon, "Multilayer silicon nitride-on-silicon integrated photonic platforms and devices," J. Lightwave Technol. **33**, 901–910 (2015).